Inorganic Chemistry

Article

pubs.acs.org/IC

Mechanism of RuO_2 Crystallization in Borosilicate Glass: An Original *in Situ* ESEM Approach

Hassiba Boucetta,*[,†] Renaud Podor,[§] Lorenzo Stievano,[‡] Johann Ravaux,[§] Xavier Carrier,[∥] Sandra Casale,[∥] Stéphane Gossé,[⊥] Amélie Monteiro,[†] and Sophie Schuller[†]

[†]CEA Marcoule, DEN/DTCD/SECM/LDMC, F-30207 Bagnols-sur-Cèze, France

[‡]ICG-AIME UMR CNRS 5253, Université de Montpellier II, F-34095 Montpellier, France

[§]Institut de Chimie Séparative de Marcoule, UMR 5257 CEA-CNRS-UM2-ENSCM, F-30207 Bagnols-sur-Cèze, France

[∥]UPMC-Université Pierre et Marie Curie, Laboratoire de Réactivité de Surface, F-75005 Paris, France

[⊥]CEA Saclay, DEN/DPC/SCCME/LM2T, F-91191 Gif-sur-Yvette, France

Supporting Information

ABSTRACT: Ruthenium, a fission product arising from the reprocessing of spent uranium oxide (UOX) fuel, crystallizes in the form of acicular RuO_2 particles in high-level waste containment glass matrices. These particles are responsible for significant modifications in the physicochemical behavior of the glass in the liquid state, and their formation mechanisms are a subject of investigation. The chemical reactions responsible for the crystallization of RuO_2 particles with acicular or polyhedral shape in simplified radioactive waste containment glass are described. *In situ* high-temperature environmental scanning electron microscopy (ESEM) is used to follow changes in morphology and composition of the ruthenium compounds formed by reactions at high temperature between a simplified RuO_2–$NaNO_3$ precursor and a sodium borosilicate glass (SiO_2–B_2O_3–Na_2O). The key parameter in the formation of acicular or polyhedral RuO_2 crystals is the chemistry of the ruthenium compound under oxidized conditions (Ru^{IV}, Ru^{V}). The precipitation of needle-shaped RuO_2 crystals in the melt might be associated with the formation of an intermediate Ru compound ($Na_3Ru^{V}O_4$) before dissolution in the melt, allowing Ru concentration gradients. The formation of polyhedral crystals is the result of the direct incorporation of RuO_2 crystals in the melt followed by an Ostwald ripening mechanism.

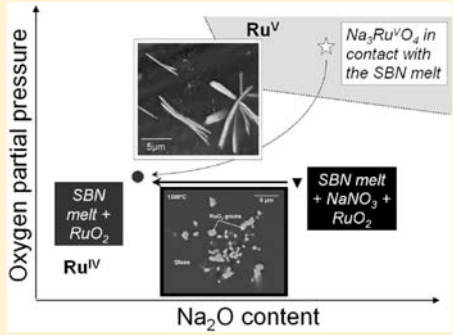

1. INTRODUCTION

Fission products and actinides arising from reprocessing of spent uranium oxide (UOX) fuel are contained in glass matrices by vitrification in an indirect induction-heated metal crucible and in the near future in a direct induction-heated cold crucible melter.[1] Nitric acid solutions containing the highly radioactive elements arising from hydrometallurgical reprocessing, together with the fines (Pd, Rh, Ru, Zr, Mo, Tc, Sn) present in metallic form after clarification, are dried and then calcined prior to vitrification. The loading limit for these elements in the glass matrix, a few weight percent for the glass synthesized in calcination–vitrification or liquid feed vitrification processes, depends more generally on the type of process (ceramic melter, direct or indirect induction-heated crucible) and requires control of the synthesis parameters (feed rate, temperature, refining time, effectiveness of stirring) and of the glass properties (composition, viscosity). The platinum-group metals (Ru, Rh, Pd) are very sparingly soluble in the glass matrix and can modify the physical and chemical properties of the containment glass and affect the process operating parameters. The crystalline phases, in the form of insoluble metal alloys (Pd–Te, Pd–Rh–Te) or oxides (RuO_2, (Rh,Ru)-O_2),[2−6] tend to accumulate at the bottom of the melter in unstirred vitrification processes[7−13] and locally increase the electrical conductivity[14] and viscosity[15,16] of the glass. During the vitrification step, reactions between ruthenium compounds and the glass precursor lead to the formation of crystalline RuO_2 and Ru metal solid solutions of various sizes and morphologies. Depending on the formation conditions (temperature, oxygen partial pressure),[2] these compounds (mainly at oxidation state +IV or 0) are very sparingly soluble[17−20] in sodium borosilicate glass matrices: they precipitate in the glass melt as Ru metal with the typical hexagonal close-packed (*hcp*) crystalline structure,[21] and RuO_2 with polyhedral[11,22,23] or acicular[6,13,15,24,25] morphologies. The latter morphology results in significant changes in glass behavior in the liquid state. This morphology found in glass produced from calcined waste and glass precursors plays a major role in increasing the local electrical conductivity[26−29] and could account for malfunctions in melters sensitive to this property.[13] This morphology also modifies the rheological behavior of glass in the liquid state[12] and may decrease the kinetics of incorporation of low-solubility fission products and actinides and thus diminish the homogeneity of the resulting glass.[30]

Received: October 5, 2011
Published: March 8, 2012

This study therefore focuses on the conditions of formation of crystallized RuO_2 phases. A mechanism was first proposed by Krause and Luckscheiter,[12] who suggested that the formation of acicular phases is initiated by the decomposition of gaseous RuO_3 obtained by oxidation of RuO_2 with sodium molybdate formed during the calcination step. In this case, RuO_2 needles form in the interstitial voids created by the glass frit before they coalesce and disperse when the frit is melted. More recently, Enokida[25] highlighted the role of sodium nitrate in the formation of acicular RuO_2. He showed that the early dissolution of RuO_2 in $NaNO_3$ leads to the formation of an intermediate Na_3RuO_4 compound, which decomposes in contact with the glass to form acicular RuO_2 phases *via* the possible formation of RuO_4.[31] On the basis of these earlier studies, we propose here to elucidate in detail the reaction mechanisms leading to the formation of the various ruthenium compounds during the synthesis of a simplified glass composition. *In situ* high-temperature environmental scanning electron microscopy (ESEM) is used to follow changes in the morphology and composition of the ruthenium compounds formed by reactions between a simplified calcine (RuO_2–$NaNO_3$) and a simplified sodium borosilicate glass precursor (SiO_2–B_2O_3–Na_2O). The solid-state microstructure of the intermediate compounds is characterized by SEM, XRD, and HRTEM. Ruthenium K-edge EXAFS spectroscopy is also used to examine the local structure of the formed phases. This combined approach provides new information on the conditions of formation of phases containing ruthenium during the synthesis of the simplified glass system, before investigating more complex systems containing the full waste spectrum of spent uranium oxide fuel.

2. EXPERIMENTAL SECTION

2.1. Sample Preparation. The compositions of two series of glass samples (SBN*x*-Compound$_y$) were selected from a benchmark composition (SBN), basically a simplified SON68 glass composition[32] defined in the ternary SiO_2–B_2O_3–Na_2O system. The synthesized compounds are designated by the composition of the reaction mixture used to obtain them as well as the synthesis method and conditions. For example, the simplified calcined waste compound designated NaRu was synthesized from $NaNO_3$ and RuO_2. The SBN1-Ru_{1300} glasses were synthesized from SBN glass frit and RuO_2, while the SBN*x*-NaRu$_y$ glasses were obtained from the SBN frit, $NaNO_3$, and RuO_2. The notation *x* indicates the number of synthesis steps, and *y* is the glass synthesis temperature. The weight of the final compound ranged from 5 to 10 g. The concentration of ruthenium dioxide (RuO_2) in the glass is on the same order of magnitude as the quantity of ruthenium in a complex glass.

The SBN glass was synthesized for 3 h at 1300 °C in a tilting resistance furnace from SiO_2 (SIFRACO Millisil, 100%), H_3BO_3 (PROLABO, 99%), and Na_2CO_3 (PROLABO, 99.9%). The following additional precursors were used in these experiments: $NaNO_3$ (PROLABO, 99.5%) and RuO_2 (HERAEUS, 98.2%).

The NaRu precursor was prepared from a mixture of $NaNO_3$ and RuO_2. RuO_2 was first dissolved with $NaNO_3$ for 1 h in an alumina crucible at 800 °C according to the protocol of Enokida.[25] This NaRu precursor is used as a simplified composition for the complex industrial calcine.

Synthesis protocols in one and two steps were developed to determine the role of $NaNO_3$ in the transformation of ruthenium in the glass. For synthesis in a single step, RuO_2 reacted directly with the glass frit for 3 h in the presence of excess $NaNO_3$ at 800 °C (SBN1-$NaRu_{800}$) and 1300 °C (SBN1-$NaRu_{1300}$), or without $NaNO_3$ (SBN1-Ru_{1300}) at 1300 °C. For the two-step synthesis, RuO_2 was first reacted with $NaNO_3$ for 1 h at 800 °C in an alumina crucible. The resulting compound (sample NaRu) was then placed in contact with the glass frit at 800 °C (SBN2-$NaRu_{800}$) or 1300 °C (SBN2-$NaRu_{1300}$) for 2 h. All of the experiments were carried out in a muffle furnace, in alumina crucibles with a heating rate of 400 °C/h. The crucibles containing the precursors were placed in the furnace after preheating to the desired temperature. The operating conditions are indicated in Table 1.

Table 1. Experimental Procedure of Ru-Containing Samples

		experimental procedure		
tests	reaction	number of steps	temperature (°C)	time (h)
NaRu	$NaNO_3$ + RuO_2	1	800	1
SBN1-Ru_{1300}	Glass frit SBN + RuO_2	1	1300	3
SBN1-$NaRu_{800}$	$NaNO_3$ + RuO_2 + Glass frit SBN	1	800	3
SBN1-$NaRu_{1300}$	$NaNO_3$ + RuO_2 + Glass frit SBN	1	1300	3
SBN2-$NaRu_{800}$	($NaNO_3$ + RuO_2) + Glass frit SBN	2	800	1 + 2
SBN2-$NaRu_{1300}$	($NaNO_3$ + RuO_2) + Glass frit SBN	2	1300	1 + 2

2.2. Experimental Analysis. Several spectroscopic and microstructural analysis methods were used to examine in detail the structure and microstructure of the various glass compositions and intermediate compounds containing ruthenium.

High-Resolution Transmission Electron Microscopy. High-resolution transmission electron microscopy (HRTEM) was performed with a JEOL JEM 2011 instrument operating at 200 kV. Finely ground samples in suspension in ethanol were deposited on a copper grid 3 mm in diameter, covered with a thin film of carbon.

Extended X-ray Absorption Fine Structure. X-ray absorption spectroscopy (XAS) measurements were carried out at the Elettra Synchrotron (Trieste, Italy) on the XAFS beamline with a Si(311) double-crystal monochromator. The electron storage ring energy and injection current were 2.00 GeV and 300 mA. Ruthenium K-edge transmission spectra were acquired by means of three ionization chambers. The absorption of the sample was detected between the first and the second chambers, whereas the absorption of a reference standard (rhodium metal) was measured between the second and the third chambers. Two to four spectra were recorded for each sample with an acquisition time of about 1 h to ensure the collection of spectra with an acceptable signal-to-noise ratio. EXAFS spectra were processed using the ATHENA software.[33,34] The Fourier transform of the EXAFS signal was calculated between 2 and 14 $Å^{-1}$. EXAFS data were fitted with ARTHEMIS software[33,34] using phases and amplitudes calculated by FEFF 6.0[35] for the RuO_2 rutile-type crystal structure (space group $P4_2/mnm$).

Scanning Electron Microscopy. Scanning electron microscope (SEM) analyses were performed with a Philips XL30 microscope operating at 15 kV. Analyses were performed on polished cross sections obtained by embedding the samples in resin and polishing them with a Struers polisher to 1 μm with a diamond disk and anhydrous suspensions to prevent the dissolution of any water-soluble phases during polishing. A conductive carbon film was then deposited on the sample surface to make it conductive. SEM images were obtained with backscattered electrons. The qualitative sample composition was determined by EDX analysis of the X-rays emitted by interaction of the sample with the SEM electron beam. The radiation emitted by the material was detected using a lithium-doped silicon crystal and quantified with IMIX software. EDX analysis is unable to detect elements lighter than carbon.

X-ray Diffraction. X-ray diffraction (XRD) measurements were carried out by means of a Philips X'Pert Pro θ–θ diffractometer with a copper anticathode at a wavelength $\lambda_{K\alpha}$ of 0.15406 nm. The samples were first ground to fine powder to reduce the possibility of preferred crystal orientation. Diffractograms were then recorded between 10° and 80° in 0.017° steps with an acquisition time of 2 s per step. Crystalline phases were identified by comparison of the diffractograms with the crystallographic databases of the International Center for Diffraction Data (JCPDS file).

In Situ High-Temperature Environmental Scanning Electron Microscopy. In situ high-temperature reactions were monitored with a FEI QUANTA 200 FEG environmental scanning electron microscope

dx.doi.org/10.1021/ic202156y | *Inorg. Chem.* 2012, 51, 3478–3489

(ESEM) operating at 30 kV.[36] The sample was placed in a 5-mm-diameter platinum crucible on a heating stage inside the microscope analysis chamber. To examine the NaRu compound behavior, excess $NaNO_3$ powder was mixed with RuO_2 powder. For SBN2-$NaRu_y$ glass, a piece of the NaRu mixture was deposited on a fragment of SBN glass frit, and for SBN1-$NaRu_y$ glass, a quantity of blended $NaNO_3$ and RuO_2 powder was deposited on a fragment of glass frit. The SBN1-Ru_{1300} sample was analyzed by depositing RuO_2 powder on a fragment of SBN frit. The specimens were heated to 900 °C for NaRu compounds and SBN*x*-$NaRu_y$ glass and 1300 °C for SBN1-Ru_{1300} glass at a heating rate of 20 °C/min in contact with steam at a pressure of 350 Pa. Continuous series of micrographs were recorded during the heating cycles. Two experiments were performed successively. First, samples were heated (and continuously observed) up to the maximal temperature in order to determine the successive phase transformations. Then other samples of the same type were heated to the characteristic transformation temperatures and cooled down to room temperature for EDX analyses of the phases formed at different steps. EDX analyses were performed with a Bruker 5010 EDS analyzer after cooling samples prepared *in situ* at characteristic temperatures. The five videos recorded during the experiments are provided in the Supporting Information.

Thermal Properties. Differential thermal analysis (DTA) and thermogravimetric analysis (TGA) were carried out by means of a Setaram TGA 92−16 thermal analyzer. This technique makes it possible to determine the transformations of the material by measuring the different thermal effects. In glass, these phenomena correspond mainly to the glass transition (endothermic effect), crystallization (exothermic effect), and melting of crystallized phases (endothermic effect). The principle of this method consists of measuring the temperature difference between the analyzed sample and an inert reference compound (alumina) with a known thermal effect in the investigated temperature range. The measurements were performed under an argon atmosphere in alumina or platinum crucibles. The sample masses were about 75 mg, and the rate of temperatures ramps was 10 °C/min.

3. RESULTS

A series of experiments was performed to obtain data in order to propose a comprehensive model for the RuO_2 morphology control during borosilicate glass melting. The videos recorded during *in situ* HT-ESEM experiments are available in the Supporting Information. The figures in the article correspond to selected views at given temperatures that are representative of the main transformations.

3.1. Characterization of the NaRu Precursor. The microstructure, morphology, and structure of the NaRu precursor were analyzed after heat treatment for 1 h at 800 °C, then cooling to room temperature. Two samples of this compound were selected for analysis: one (NaRu-top) was selected from the top part of the crucible and represents the supernatant fraction of the precursor which solidifies during cooling to room temperature. The second sample (NaRu-bottom), possibly containing solid phases precipitated in the hot nitrate melt, was selected from the bottom part of the crucible.

The SEM results coupled with EDS analysis of NaRu-top indicate the presence of a uniform phase on the micrometer scale with light contrast, composed of ruthenium, sodium and oxygen (Figure 1a). XRD analysis of the bulk sample indicates the

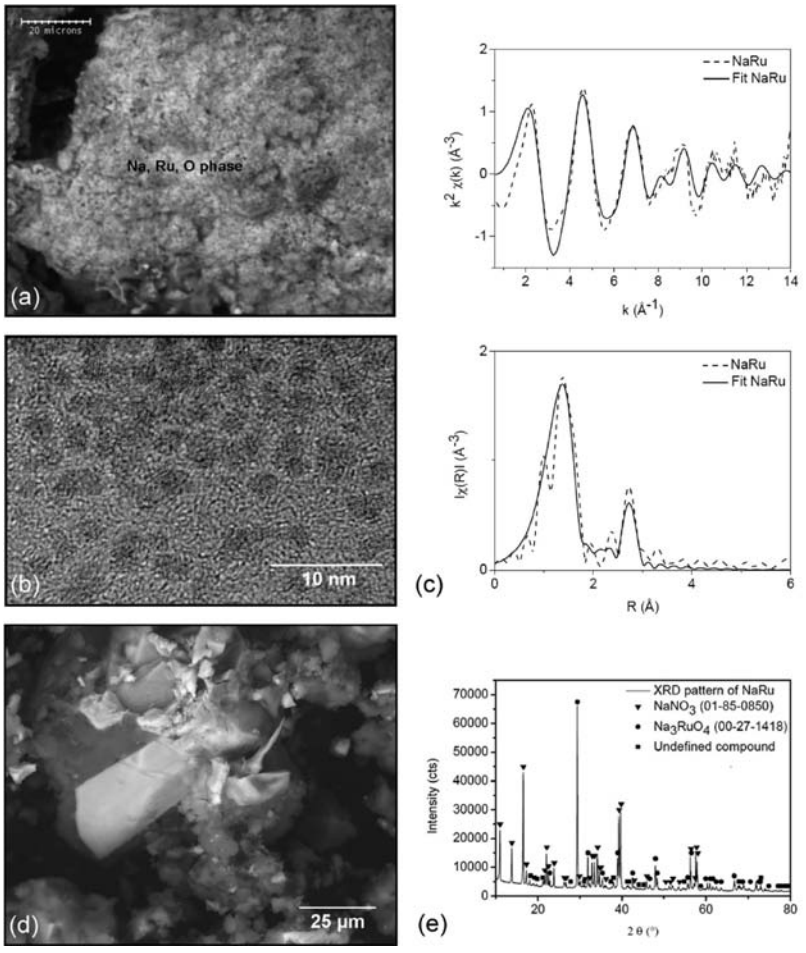

Figure 1. SEM (a) and HRTEM (b) micrographs and EXAFS spectrum and relative Fourier transform (c) of the NaRu-top sample cooled to room temperature and ESEM image (d) and XRD spectrum (e) of NaRu-bottom sample cooled to room temperature.

dx.doi.org/10.1021/ic202156y | *Inorg. Chem.* 2012, 51, 3478−3489

dominant presence of $NaNO_3$ with a hexagonal structure and $NaNO_2$ with an orthorhombic structure (cf. Supporting Information, file S1). No known crystalline phase containing ruthenium could be detected in the diffractogram of NaRu-top. The absence of diffraction peaks other than those of $NaNO_3$ and $NaNO_2$ suggests that in this part of the sample, ruthenium is present in poorly crystallized, nanoparticulate, or amorphous phases. On a smaller scale, the presence of monodisperse crystalline nanoparticles of about 2 nm homogeneously distributed in the sodium nitrate matrix was detected by transmission electron microscopy (Figure 1b). The crystalline nature of these particles was determined by the presence of fringes typical of the presence of ordered crystal planes. The distance between planes is about 2.2 Å (±0.1) corresponding to the distance between two (111) planes in the crystalline phase of RuO_2 with a rutile structure, which crystallizes in the tetragonal system, space group $P4_2/mnm$.[37] This result was confirmed by the EXAFS spectrum of this sample and its Fourier transform (Figure 1c). The spectra are fitted satisfactorily by two first-neighbor oxygens at about 1.95 Å (Ru−O distance) and a Ru second neighbor at 3.08 Å (Ru−Ru distance). These values, very close to the distances typically observed in the crystal structure of RuO_2,[37] indicate the presence of the RuO_2 structure. However, given the absence of successive shells in the Fourier transform and the high values of the Debye−Waller factor σ^2 (larger than 0.006 Å^2) for the observed shells (cf. Table 2), the RuO_2 has no long-range order. All of these results are in line with the reprecipitation of poorly ordered crystalline nanoparticles of RuO_2 in the bulk NaRu material during cooling of the melt to room temperature.

Table 2. EXAFS Results at the Ru K-Edge for NaRu and SBN$_x$-NaRu$_y$ Glasses: Interatomic Distances, Reduction Amplitude Factor (S_0), Energy Difference (ΔE_0), and Debye Waller Factors (σ^2)

sample	bonding	interatomic distance (Å)	S_0	ΔE_0 (eV)	σ^2 (Å^2)
NaRu	$Ru-O_1$	1.95	1.00	−2.12	0.0061
	$Ru-O_2$	1.99			0.0061
	$Ru-Ru_1$	3.12			0.0047
SBN1-NaRu$_{800}$	$Ru-O_1$	1.96	1.14	−0.62	0.0024
	$Ru-O_2$	2.00			0.0024
	$Ru-Ru_1$	3.15			0.0041
	$Ru-Ru_2$	3.56			0.0030
	$Ru-Ru_3$	4.50			0.0039
SBN1-NaRu$_{1300}$	$Ru-O_1$	1.96	1.05	−0.05	0.0022
	$Ru-O_2$	2.00			0.0022
	$Ru-Ru_1$	3.13			0.0038
	$Ru-Ru_2$	3.57			0.0027
	$Ru-Ru_3$	4.51			0.0049
SBN2-NaRu$_{800}$	$Ru-O_1$	1.96	1.07	0.30	0.0028
	$Ru-O_2$	2.00			0.0028
	$Ru-Ru_1$	3.16			0.0052
	$Ru-Ru_2$	3.56			0.0033
	$Ru-Ru_3$	4.50			0.0053
SBN2-NaRu$_{1300}$	$Ru-O_1$	1.95	0.97	0.50	0.0022
	$Ru-O_2$	2.00			0.0022
	$Ru-Ru_1$	3.15			0.0035
	$Ru-Ru_2$	3.57			0.0027
	$Ru-Ru_3$	4.52			0.0036

The SEM micrograph (Figure 1d) and XRD pattern of the second sample taken from the NaRu precursor, i.e., sample NaRu-bottom (Figure 1e), confirms the presence of a new mixed Na−Ru phase, Na_3RuO_4, in addition to the typical profiles of $NaNO_3$ and $NaNO_2$. Na_3RuO_4[38] contains Ru(V) and is probably formed through the reduction of nitrates in the melt. These results agree well with those of Enokida,[25] who reported that, at the temperature of preparation of the NaRu precursor, the Na_3RuO_4 compound is in equilibrium with the $NaNO_x$ melt and that liquid $NaNO_3$ (probably mixed with $NaNO_2$ considering the reported preparation conditions) can dissolve about 6 wt % Ru at T = 800 °C.

In situ high-temperature environmental SEM monitoring of the reaction between ruthenium dioxide and sodium nitrate made it possible to determine the formation mechanism of the Ru compound (cf. Supporting Information, file S2). A mixture of RuO_2 with $NaNO_3$ with the same composition as the NaRu precursor was deposited in the high-temperature device associated with the ESEM at room temperature (Figure 2a). This mixture was heated to 850 °C in the ESEM chamber. A first reaction was observed at T = 285 °C, probably corresponding to the melting of $NaNO_2$ obtained by surface decomposition of $NaNO_3$. Melting of $NaNO_3$ was systematically observed in the temperature range 302−306 °C. Those two temperatures were confirmed by DTA, which revealed two endothermic reactions at 282 and 325 °C (cf. Supporting Information, file S3) corresponding to the melting temperatures of the $NaNO_3$−$NaNO_2$ mixture and $NaNO_3$[39] (Tm = 308 °C). At this temperature, solid RuO_2 started to disperse in the molten nitrate and formed particle aggregates containing ruthenium from about 445 °C (Figure 2b). After subsequent growth, dissolution of the RuO_2 crystals in the liquid was then observed. This reaction was followed by the growth of large well-defined crystals of approximately 5−10 μm associated with the denitration of a part of the liquid at 600 °C (Figure 2c). SEM/EDS analyses performed on these crystals after cooling to room temperature shows that they contain both ruthenium and sodium with a Na/Ru ratio of 3. Combining this observation with the XRD results obtained for sample NaRu-bottom, we can safely attribute the growth of these crystals to the precipitation of Na_3RuO_4. Together with the crystals of Na_3RuO_4, the analysis by SEM/EDS also revealed the presence of RuO_2 crystals of about 200 nm.

The complete decomposition/evaporation of the residual liquid occurs between 600 and 670 °C, leading to the formation of a solid containing $Na_3Ru^VO_4$ (Figure 2d). This solid begins to decompose at 350 Pa at T = 710 °C (humid atmosphere) to 770 °C at 350 Pa in the air (Figure 2e) and leads to the formation of a mixed Na−Ru phase with a granular texture[40,41] at 820 °C (Figure 2f).

These *in situ* ESEM observations, combined with the *ex situ* results obtained by XRD and EXAFS on the cooled samples, provide a clear picture of the nature of the NaRu precursor. After cooling to room temperature, this material consists principally of a mixture of $NaNO_3$−$NaNO_2$ (the ratio between the two compounds depends on the calcination time at the NaRu precursor synthesis temperature) containing RuO_2 nanocrystals and Na_3RuO_4 crystals. The Na_3RuO_4 crystals are not homogeneously distributed in the NaRu precursor but tend to precipitate beneath it.

3.2. Reactivity between the NaRu Precursor and the Glass. The reactions between the NaRu precursor and SBN glass frit were observed during heating *in situ* in the ESEM (cf. Supporting Information, file S4). The data obtained were used to specify the formation steps of ruthenium compounds in the glass. The NaRu precursor previously deposited on the

dx.doi.org/10.1021/ic202156y | Inorg. Chem. 2012, 51, 3478−3489

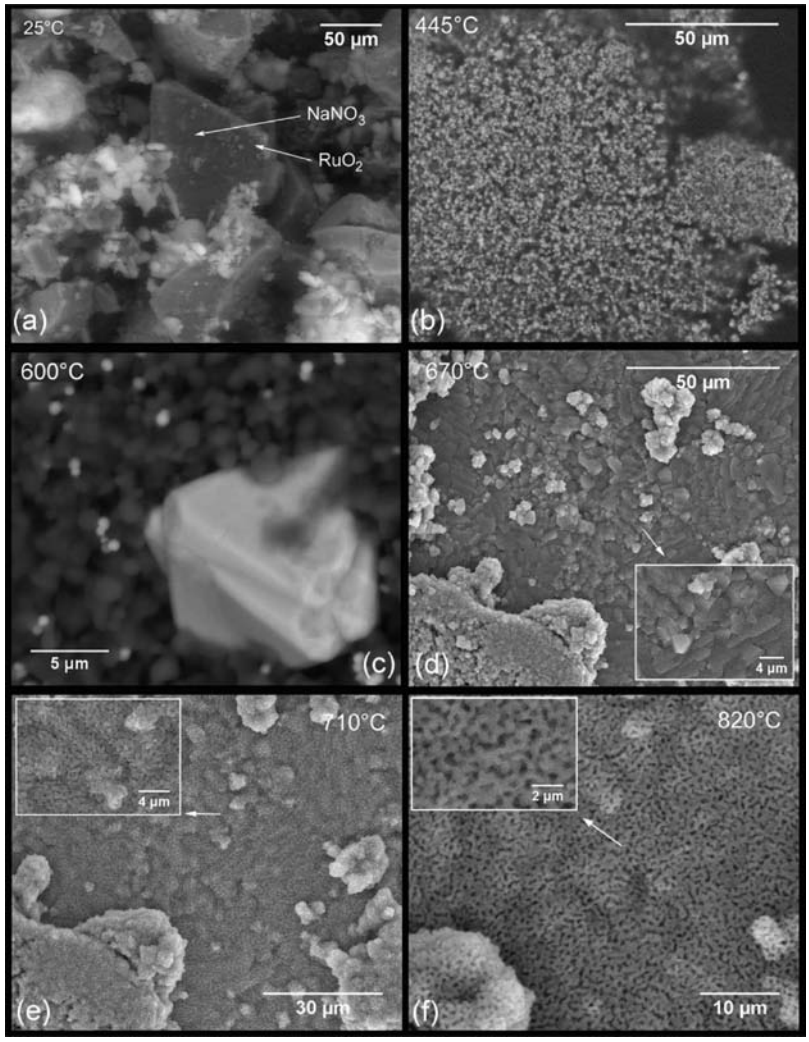

Figure 2. *In situ* observations obtained by ESEM of NaRu precursor sample at room temperature 25 °C (a) showing clusters with growth of particles containing ruthenium from 445 °C (b) to 600 °C (c). The $NaNO_3$ liquid decomposition associated with the Na_2O reaction with RuO_2 yields the formation of a single Na_3RuO_4 phase at $T \sim 670$ °C (d); then this solid begins to decompose at 710 °C, (e) followed by the formation of a mixed Na−Ru phase at 820 °C (f).

SBN glass frit at room temperature (Figure 3a) became liquid at about 225 °C. At this stage, the ruthenium-containing particles initially present in the NaRu compound were dispersed in the $NaNO_2$−$NaNO_3$ mixture (at 230.5 °C),[42] which spread and diffused on the surface of the glass matrix (Figure 3b). At the melting temperature of $NaNO_3$ (306 °C; Figure 3c), compounds with different chemical contrasts were observed on the glass surface (Figure 3d). Semiquantitative EDX analysis after cooling of a sample observed at 389 and 449 °C revealed the presence of a mixed sodium ruthenium compound, probably Na_3RuO_4 (Figure 4a,b). In the same temperature range, urchin-shaped crystalline sodium silicate phases (Figure 4a,c) and elongated sodium borate crystals were observed over the entire glass surface. The formation of these phases at temperatures below the glass transition temperature (Tg = 571 °C; Figure 5a) and their very rapid growth demonstrate the very fast diffusion of sodium and variation of the local composition at the glass surface. The formation of such compounds (but not with the same morphology) has been reported by Abe et al.[39] during the reactions occurring in the $NaNO_3$−B_2O_3 and $NaNO_3$−SiO_2 systems. The sodium silicate and borate phases observed at 445 °C (Figure 3e) began to dissolve in the glass matrix at 700 °C (Figure 3f). At this temperature, a significant release of gas was observed. The pores observed in the glass surface are interpreted as evidence of escaping gas. The glass—initially solid and heterogeneous on the surface—became homogeneous in the liquid volume around 750 °C. This reaction corresponds to the denitration of the mixture of $NaNO_3$ and $NaNO_2$ during the reaction with glass. The temperature of this reaction as determined by environmental SEM was correlated with the value obtained by differential thermal and thermogravimetric analysis. The thermogram (Figure 5b) reveals an endothermic variation at 685 °C associated with a mass loss corresponding to the decomposition of the mixture of $NaNO_3$ and $NaNO_2$ of 9.85 mg (59.48 wt %). Above this temperature, ruthenium compounds are dispersed in the molten glass. EDS analyses performed on several particles embedded in the glass cooled at room temperature revealed only the presence of RuO_2 particles.

Microstructural characterization of the phases formed after the reaction between NaRu and a SBN glass frit at 800 °C and observed after cooling (sample SBN2-$NaRu_{800}$) revealed the presence of micrometric RuO_2 needles with tetragonal structure, dispersed or aggregated in the glass matrix of 20−50 μm diameter (Figure 6a). Sample SBN2-$NaRu_{1300}$, prepared

dx.doi.org/10.1021/ic202156y | *Inorg. Chem.* 2012, 51, 3478−3489

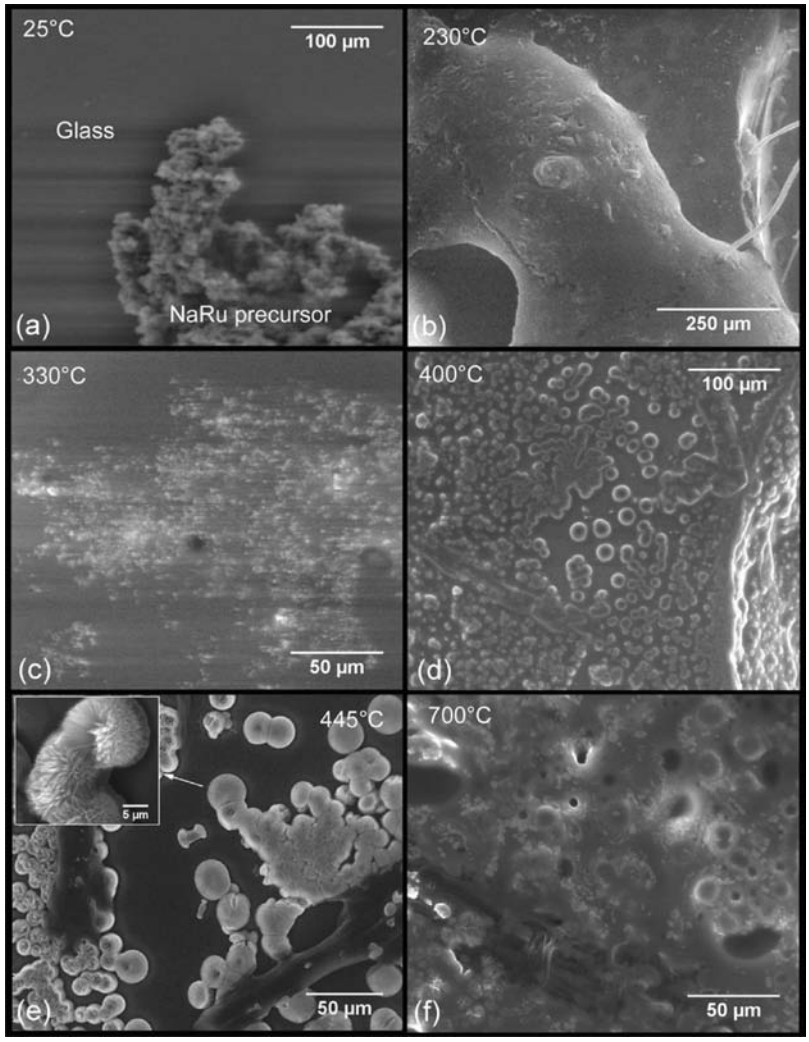

Figure 3. ESEM images obtained during *in situ* HT-ESEM heat treatment of the NaRu precursor sample deposited on the SBN glass surface. An image of this assembly at room temperature is shown in part a. Spreading of NaRu on the surface of the SBN glass begins at a temperature below 230 °C (b); the chemical contrast observed on the glass surface at 330 °C corresponds to the Ru particles dispersion in the $NaNO_3$–$NaNO_2$ liquid (c). This liquid reacts with SBN glass at $T \sim 400$ °C (d) to form borate and silicate phases at 445 °C (e). When $T \geq 700$ °C, the silicate and borate phases react with SBN glass, which begins to melt. The pores that form at the glass surface correspond to the release of gas from denitration (f).

according to the same procedure and heat-treated at 1300 °C, also contained RuO_2 needles about 40-μm-long, substantially larger than those obtained at 800 °C (Figure 6b). EXAFS analysis clearly shows the presence of crystalline RuO_2 in both samples since all Ru–O and Ru–Ru distances and peak intensities (Table 2) agree very well with the theoretical values obtained from the crystallographic structure of RuO_2.[37] The Debye–Waller factors of the different spectral paths decrease regularly from sample SBN2-$NaRu_{800}$ to sample SBN2-$NaRu_{1300}$ (Table 2), which is consistent with the increased crystallinity of RuO_2 and the presence of larger crystals (Figure 6b) in the glass synthesized at 1300 °C.

3.3. Direct Incorporation of Ruthenates in the Glass Frit. A few micrograms of the Na_3RuO_4 crystal obtained from the reaction between $NaNO_3$ and RuO_2 in the ESEM chamber at $T = 720$ °C (cf. section 3.1) were deposited on the surface of a piece of SBN glass frit, in the HT device of the ESEM chamber, and heated up to 845 °C under 350 Pa in the air (Figure 7a; cf. Supporting Information, file S5). No reaction occurs up to $T = 520$ °C (Figure 7a). At this temperature, the $Na_3Ru^VO_4$ crystals begin to react with the glass, and an intermediate phase begins to form at the $Na_3Ru^VO_4$–SBN glass interface. This phase is shown by the arrow in Figure 7b. The nature of the new intermediate phase formed at the surface of the glass could not be determined. This reaction becomes faster at temperatures higher than 670 °C and locally decreases the melting temperature of the SBN glass frit (Figure 7c). At about 750 °C, the $Na_3Ru^VO_4$ crystals are clearly starting to dissolve in the melt (Figure 7d). Heating this sample for 45 min at 840 °C followed by rapid cooling to room temperature leads to the formation of needle-shaped RuO_2 crystals in the glass (Figure 7e). The EDS analysis of the composition of the glass near these RuO_2 crystals shows that in this region the glass is enriched in Na_2O compared to the initial SBN composition. Furthermore, very small needle crystals less than 100 nm in diameter are present near the large needle crystals (Figure 7f). These very small crystals might result from the precipitation during cooling to room temperature of ruthenium species still dissolved in the glass melt at high temperature.

Complementary optical microscopy observations indicate that the glass is yellow in this zone and that small bubbles are also formed close to these particles. This observation might

dx.doi.org/10.1021/ic202156y | *Inorg. Chem.* 2012, 51, 3478–3489

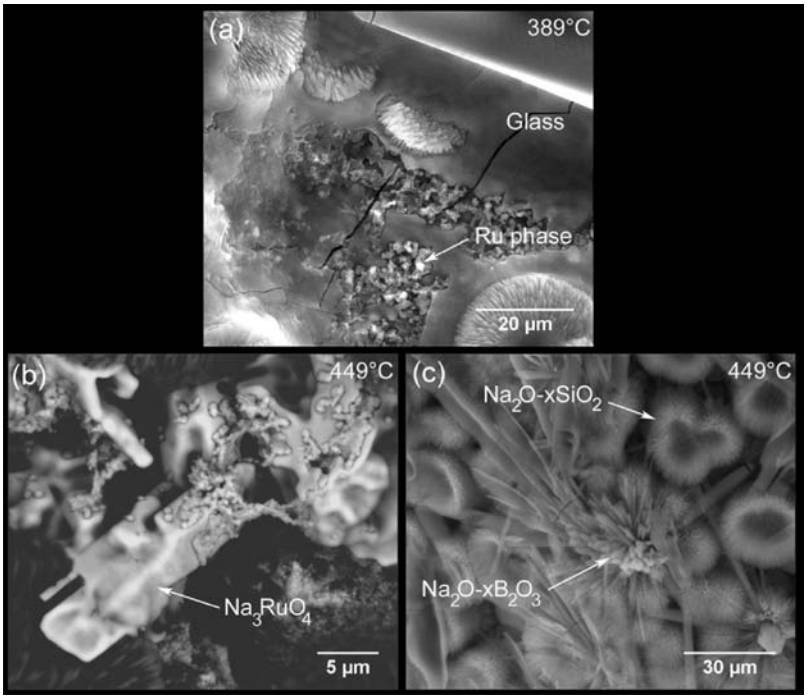

Figure 4. ESEM images recorded after quenching of the NaRu precursor and SBN glass mixture heat treated up to 389 °C (a) and up to 449 °C (b,c). Phase compositions determined by semiquantitative EDX analyses are identified at specific locations.

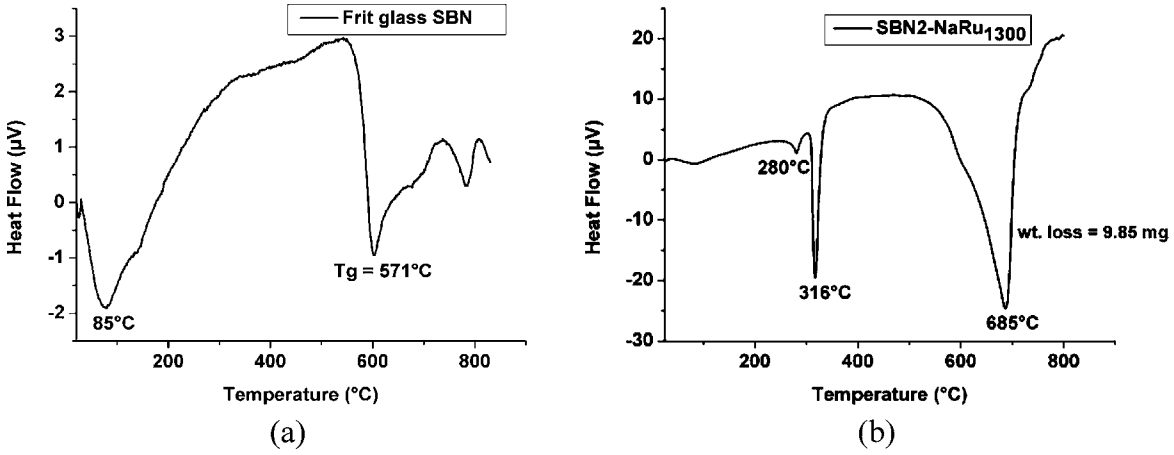

Figure 5. Differential thermal analyses (DTA) of SBN glass (a) and of the reaction between a NaRu sample and SBN glass (b) during a temperature ramp of 10 °C/min.

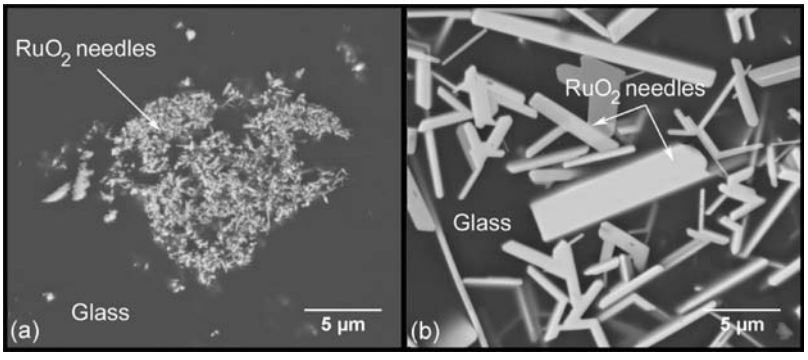

Figure 6. SEM images and EDX analyses of SBN2-$NaRu_{800}$ (a) and SBN2-$NaRu_{1300}$ (b) glasses after heat treatment at 800 and 1300 °C respectively and sample quenching at room temperature.

dx.doi.org/10.1021/ic202156y | *Inorg. Chem.* 2012, 51, 3478–3489

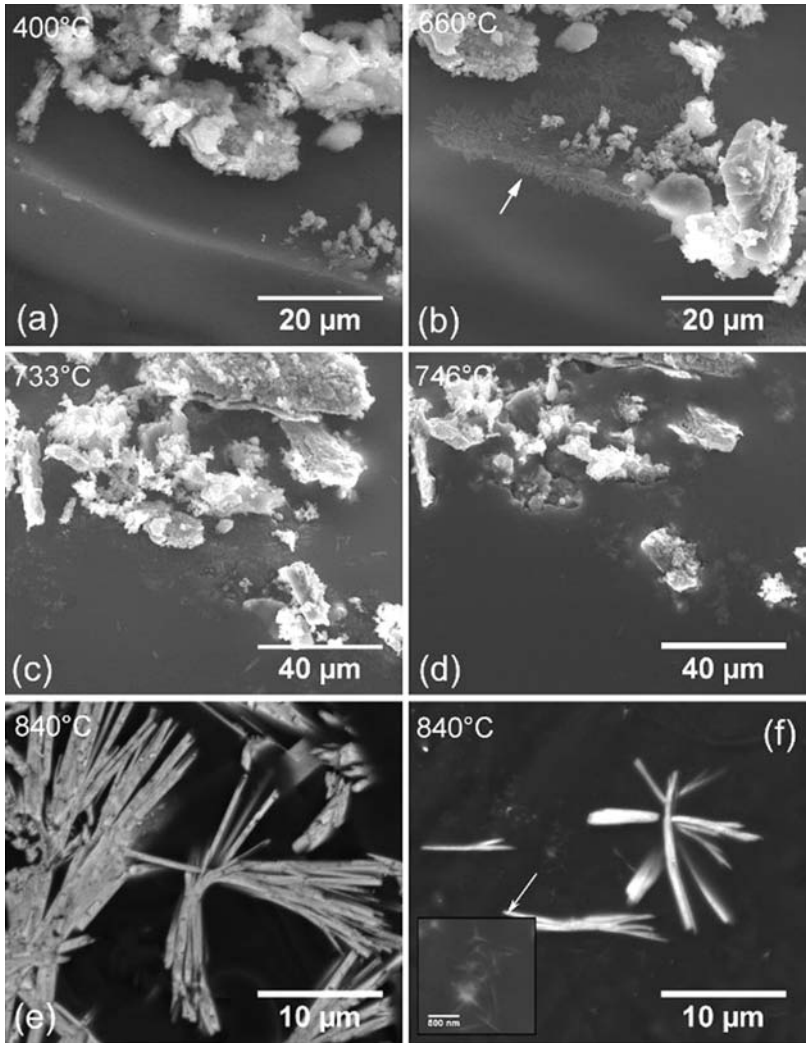

Figure 7. ESEM images recorded during *in situ* heat treatment of a sample where Na_3RuO_4 crystals are directly deposited on the SBN frit glass surface. No reactivity between the phases is observed up to 520 °C. The image recorded at T = 400 °C is representative of what is observed in the 25−520 °C temperature range (a). Sample after the beginning of the reaction between Na_3RuO_4 and the SBN glass—the arrow indicates the location of the intermediate phase—at 660 °C (b). Incorporation of the Na_3RuO_4 crystals in the SBN melt at 733 °C (c) and 746 °C (d). Needle-like shape of the RuO_2 crystals formed at T = 840 °C, observed after rapid sample cooling to room temperature (e). Observation of very small crystals between the larger RuO_2 crystals (f).

indicate that at high temperatures the glass frit still contains dissolved Ru^V, which reduces to Ru^{IV} and then precipitates as ruthenium oxide during cooling to room temperature. The reduction of Ru^V can be explained by the direct oxidation of oxide anions to O_2, which might then remain sequestrated in the glass, forming the observed bubbles.

3.4. Direct Incorporation of RuO_2 in the Glass. A specific experiment was performed directly between the SBN glass frit and RuO_2 (SBN1-Ru_{1300} sample) to determine how RuO_2 is directly incorporated in the melt (cf. Supporting Information, file S6). After heating at T = 1300 °C, the SBN1-Ru sample contains polyhedral RuO_2 with a well-ordered tetragonal structure. *In situ* high-temperature observation by ESEM of the reaction of RuO_2 with the glass frit up to 1200 °C reveals very low reactivity between these compounds. Indeed, the RuO_2 particles initially deposited on the glass surface remain at the melt surface up to approximately 850 °C (see for example Figure 8a at 167 °C). The RuO_2 particles are incorporated in the melt only at about 950−1000 °C (see Figure 8b at 943 °C).[43] The particles are then dispersed in the silicate melt at 1200 °C, and polyhedral RuO_2 particles are found once the sample is cooled to room temperature.

3.5. Direct Incorporation of a Mixture of RuO_2 and $NaNO_3$ in the Glass. The effect of the direct addition of $NaNO_3$ on the incorporation of RuO_2 in the glass was studied by performing the direct reaction between a thoroughly blended physical mixture of $NaNO_3$, RuO_2, and glass frit at T = 800 °C (SBN1-$NaRu_{800}$) and T = 1300 °C (SBN1-$NaRu_{1300}$). Analyses of the two samples after cooling to room temperature revealed the presence of polyhedral RuO_2 particles with a tetragonal structure (Figure 9) with sizes ranging from 1.5 to 5 μm, much larger than the ruthenium oxide particles used as the precursor (particle size range: 100 nm to 1 μm). The EXAFS spectra of samples SBN1-$NaRu_{800}$ and SBN1-$NaRu_{1300}$ and the corresponding Fourier transforms confirm the presence of very well ordered and crystallized RuO_2 particles in both samples. In fact, satisfactory fits (cf. Supporting Information, file S7) can be obtained up to 5 Å using the first six Ru−O and Ru−Ru shells of the RuO_2 crystal structure, revealing only very slight differences

dx.doi.org/10.1021/ic202156y | *Inorg. Chem.* 2012, 51, 3478−3489

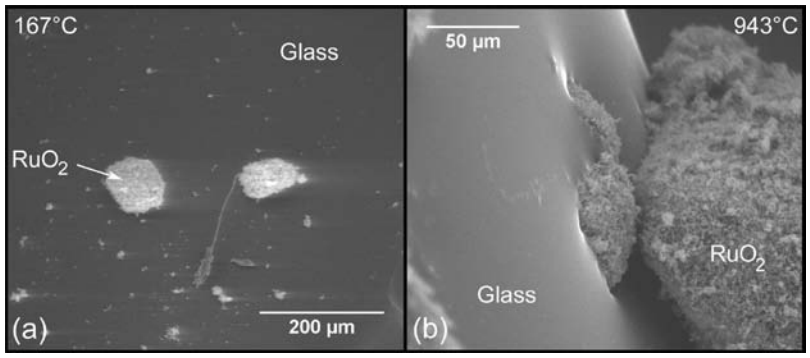

Figure 8. ESEM images showing a low reactivity between RuO_2 and SBN glass at 167 °C (a) and 943 °C (b).

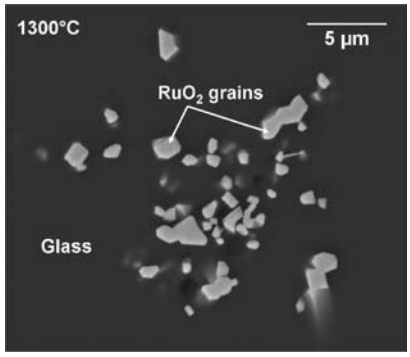

Figure 9. SEM analysis of SBN1-$NaRu_{1300}$ glass with RuO_2 grain shaped after thermal treatment at 1300 °C.

between the Debye−Waller factors of the two samples (Table 2), in agreement with a high crystalline order starting from 800 °C.

This experiment was also performed *in situ* in the HT-ESEM chamber (cf. Supporting Information, file S8). Melting of the mixture of $NaNO_3$ and $NaNO_2$ is first observed at T = 225 °C, followed by the melting of $NaNO_3$, which starts to spread over the surface of the glass particles. At increasing temperatures, the formation of urchin-like Na_2O-SiO_2 phases and the crystallization of $Na_2O-B_2O_3$ needles are observed. RuO_2 does not react either with liquid $NaNO_3$ or with the glass, and the formation of the Na_3RuO_4 crystals could not be observed. At higher temperatures, Na_2O-SiO_2 and $Na_2O-B_2O_3$ phases dissolve again in the melt. The only crystalline phase observed at this point is represented by the crystals of RuO_2 precipitated in the glass melt. Their polyhedral form is consistent with the observations made after *ex situ* experiments.

4. DISCUSSION

Figure 10 summarizes the different processes described in section 3 (Results) and discussed below.

4.1. Chemistry of Ruthenium in Silicate Melts. The chemistry of multivalent elements in silicate melts depends on both melt basicity and oxygen fugacity. These two parameters control the nature of the polyoxoanion (or polyoxocations) present in the melt as well as the oxidation degree of the studied element.[44−48] Ruthenium can be present in oxides at oxidation states III ($Ru(OH)_3$), IV (RuO_2, Na_2RuO_3), V (Na_3RuO_4), VI (Na_2RuO_4), and VIII (RuO_4).[49] In silicate melts, this element is generally reported to be stable at oxidation states 0 (Ru metal)[50] and Ru^{IV}.[22] The presence of Ru^{III} is very seldom reported.[51] The solubility of these species is generally limited from a few parts per million to hundreds of parts per million.[7,18,52] The +VI oxidation state of Ru is reported to exist in basic silicate glasses.[53,54] However, Schreiber et al.[22] reported that only the +IV oxidation state is stable for Ru in borosilicate melts.

Khedim et al.,[45−47] who worked specifically on the chemical state of chromium in basic melts, showed that higher oxidation states can be stabilized under high oxygen partial pressure. Thus, we propose here to describe the chemistry of ruthenium in borosilicate melts in a predominant species diagram (Figure 11) as a function of the oxygen pressure in equilibrium with the melt. As an example, in this diagram, the point corresponding to the initial SBN melt is shown by the dark gray circle. We will use this representation to determine and explain the mechanisms leading to the formation of polyhedral or acicular RuO_2 crystals.

4.2. Mechanism of Formation of Polyhedral RuO_2 Crystals in the Silicate Melt. *Role of RuO_2.* When added to the SBN melt, RuO_2 does not modify either the composition (expressed in O^{2-} activity) or the oxygen partial pressure of the melt. The position of the SBN melt in the predominant species diagram (Figure 11) is not modified (dark gray circle). The RuO_2 crystals (melting point =1200 °C) dissolve in the SBN melt until Ru^{IV} saturation is reached and the remaining RuO_2 crystals no longer react. This process continues until the sample is homogeneous through convection of the RuO_2 nanocrystals in the melt and saturation of the melt into Ru^{IV} species. Then, small RuO_2 particles that are initially dispersed in the glass dissolve and generate local supersaturation with regard to ruthenium. Ruthenium then diffuses in the glass, precipitates, and leads to the growth of larger RuO_2 particles on the glass (this hypothesis is supported by HRTEM observations that showed the presence of particles a few nanometers in diameter). This mechanism, summarized in Figure 12a, corresponds to classical Ostwald ripening,[55] as already reported by Pflieger et al.[23] The formation of polyhedral crystals, generally associated with the Ostwald ripening mechanism, can also be obtained during synthesis performed in molten salts.[56,57]

Role of $NaNO_3$ Addition to RuO_2. The addition of $NaNO_3$ to the SBN melt leads to Na_2O enrichment of the initial melt. The point representing the SBN melt with $NaNO_3$ is thus shifted to higher O^{2-} activities in the diagram of predominant Ru species in borosilicate melts (triangle in Figure 11). The position of this point on the pO_2 axis depends on the decomposition mechanism of $NaNO_3$. The decomposition of $NaNO_3$ forms Na_2O, which reacts rapidly with the glass (SiO_2 and B_2O_3). This reaction occurs at the surface of the melt, and the gaseous species generated are not incorporated into the formed phases. Thus, the pO_2 remains constant during the $NaNO_3$ reaction with the SBN melt. As a consequence, the addition of $NaNO_3$ to the SBN melt only

dx.doi.org/10.1021/ic202156y | Inorg. Chem. 2012, 51, 3478−3489

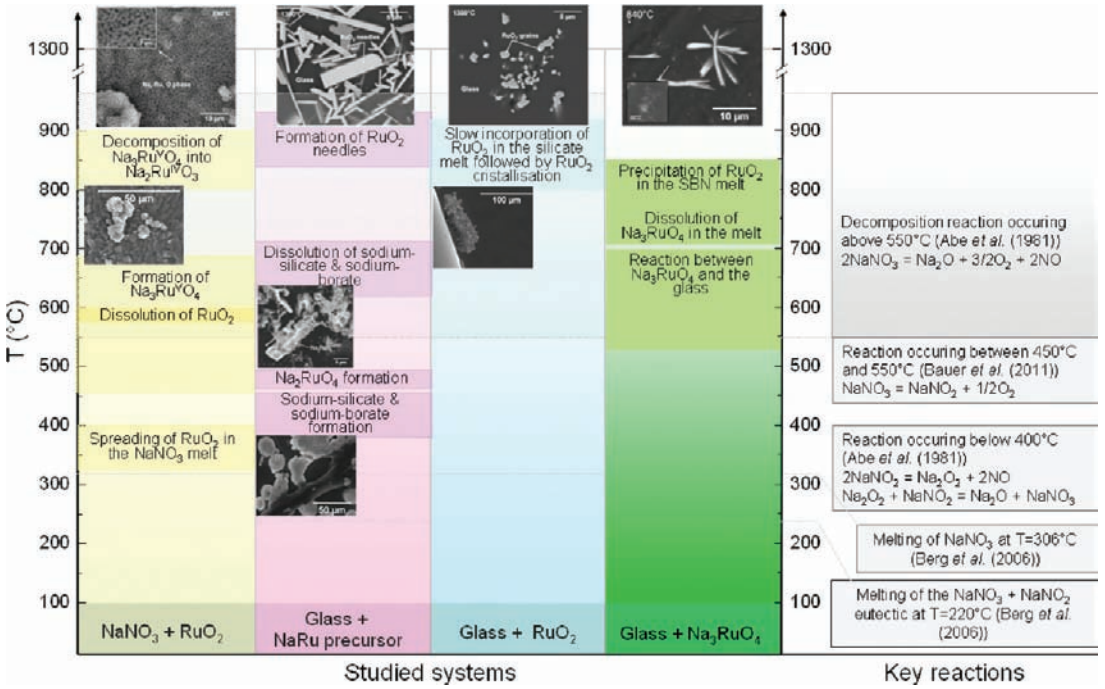

Figure 10. Summary of the different mechanisms of RuO_2 transformations in borosilicate glass.

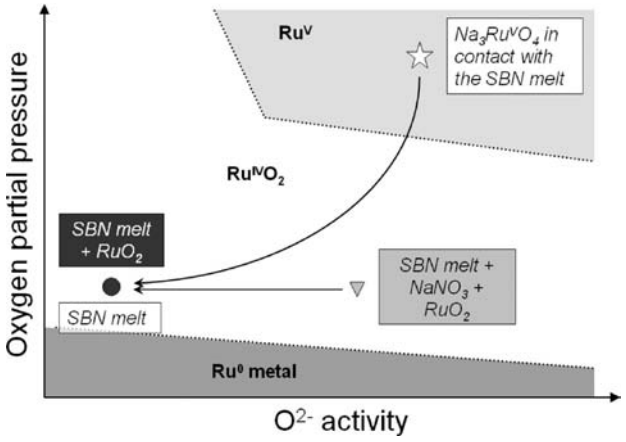

Figure 11. Schematic diagram of predominant Ru species in borosilicate melt as a function of O^{2-} (Na_2O) activity and oxygen partial pressure. The dark gray circle represents the position of the SBN melt, as well as the position of the SBN melt + RuO_2 mixture. The gray triangle represents the position of the SBN melt with $NaNO_3$ + RuO_2. The white star represents the composition of the SBN melts with Na_3RuO_4 crystals. The lines (or curves) with arrows represent the reaction paths from the initial mixture to the final homogeneous melt composition.

corresponds to a local increase of O^{2-} activity and has no influence on the local oxygen partial pressure of the melt.

Similarly, the addition of RuO_2 to the $NaNO_3$ + SBN melt does not modify either the composition or the oxygen fugacity of the melt. The point representing this composition in Figure 11 is the same as for the $NaNO_3$ + SBN melt. This composition remains in the domain where the solubility of RuO_2 in the borosilicate melt is low. Glass synthesis performed with $NaNO_3$ + RuO_2 + SBN by one reaction step without preliminary dissolution between $NaNO_3$ and RuO_2 is thus carried out without significant variations of the Ru^{IV} solubility in the melt. The return to the SBN equilibrium point is described by the composition path between the $NaNO_3$ + RuO_2 + SBN melt and the SBN + RuO_2 melt (path represented by a gray line in Figure 11). Therefore, the RuO_2 crystallization process is the same as that described in Figure 12a, i.e., a slow dissolution of the small RuO_2 particles and crystallization onto larger crystals.

4.3. Mechanism of Formation of Acicular RuO_2 Crystals in the Silicate Melt—Role of the Na_3RuO_4 Phase. Acicular RuO_2 crystallization in the SBN melt is observed when ruthenium is initially present in compounds with an oxidation state higher than IV (Ru(V) in Na_3RuO_4). The results of the experiment performed using Na_3RuO_4 suggest a mechanism of acicular RuO_2 crystallization.

When Na_3RuO_4 is added to the SBN melt, its composition is shifted to higher O^{2-} activity values and to higher pO_2 values. This corresponds to the white star position in Figure 11. During their studies of chromium chemistry in molten silicates, Khedim et al.[45−47] determined that high oxidation state polyoxoanions (CrO_4^{2-}) are more soluble than Cr^{III} in oxidized basic melts. Similarly, in the case of Ru, we might expect that the solubility of Ru^V in an oxidized basic melt (position of the white star in Figure 11) is higher than that of Ru^{IV} in the initial SBN melt (position of the dark gray circle in Figure 11). This assumption is supported by the presence of very small RuO_2 crystals in the Na_2O enriched glass after cooling that could have formed by precipitation from a saturated melt into Ru^V species (Figure 7e). Equilibrium with the SBN melt after complete dissolution and homogenization, resulting in lower composition gradients (Na_2O content, Ru^V) and pO_2 values, consequently allows local saturation of Ru^{IV} species (composition path represented by the bold curve in Figure 11).

As reported by Khedim et al. (see Figure 12 of this work)[58] for chromite crystallization, we propose that the formation of acicular RuO_2 crystals oriented perpendicularly (Figure 12b—step 3 RuO_2 crystal needle shape) is due to the pO_2 gradient during the reduction of Ru^V in the melt. When equilibrium is reached, the acicular crystals can be dispersed into the melt by

dx.doi.org/10.1021/ic202156y | Inorg. Chem. 2012, 51, 3478−3489

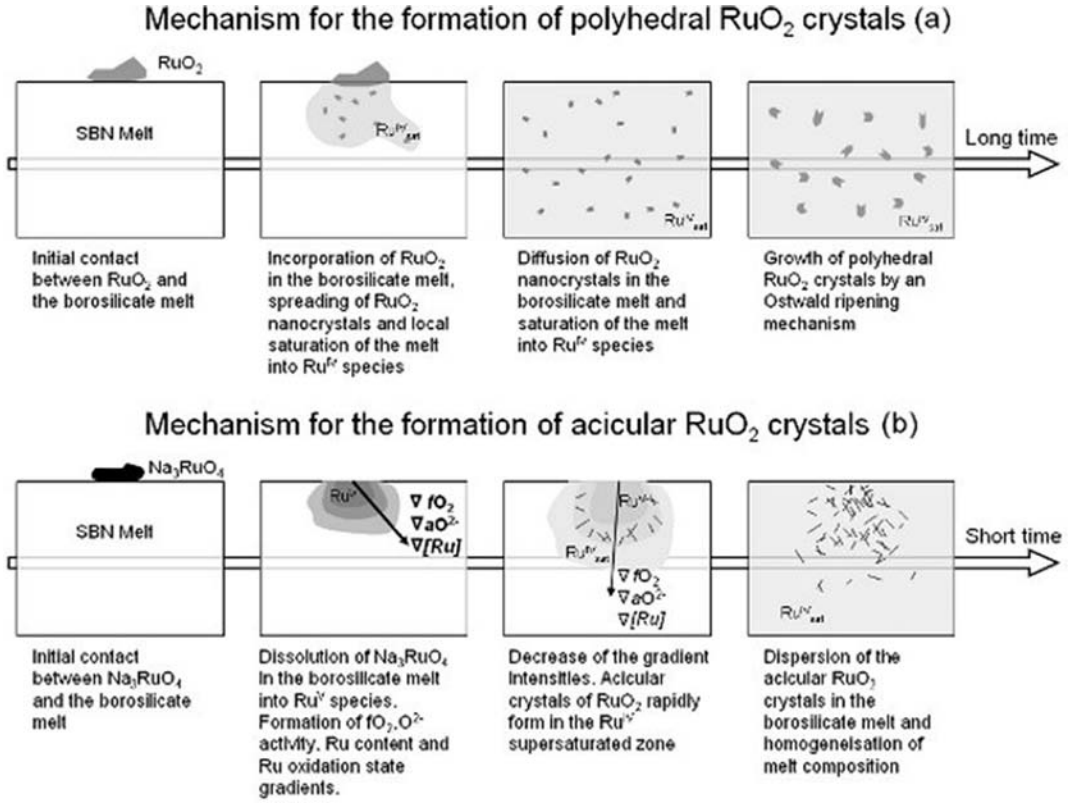

Figure 12. Mechanisms for the formation of (a) polyhedral RuO_2 crystals and (b) acicular RuO_2 crystals in the SBN borosilicate melt.

convection (Figure 12b—step 4) and then grow according to an Oswald ripening mechanism (Figure 12a, steps 3 and 4).

The process with the NaRu precursor, which contains both Na_3RuO_4 crystals together with a majority of RuO_2 dissolved in the nitrate/nitrite melt, is similar to the one described for the pure Na_3RuO_4 compound. Indeed, acicular crystals are obtained when the precursor is heated with the SBN glass. Enokida[25] also reported the formation of needle-like RuO_2 crystals under the same conditions and put forward another hypothesis for the formation of acicular RuO_2 crystals. He proposed that acicular RuO_2 crystallization results from the formation of gaseous RuO_4 during the decomposition of Na_3RuO_4. No proof for the formation of RuO_4, and consequent direct formation of RuO_2 needles has been evidenced during the present study to confirm Enokida's hypothesis. On the contrary, the direct observation of the Na_3RuO_4 crystals deposited on the surface of the glass shows that the shape of these crystals is not modified up to their incorporation by local melting of the glass, indicating that there is no decomposition of the Na_3RuO_4 crystals but simple dissolution of this compound as the glass melts. In this way, some Ru^V remains most probably dissolved in the glass melt, leading to the creation of a Ru-enriched zone, as evidenced by the precipitation of small particles of Ru-containing phases after cooling. We therefore propose that acicular RuO_2 crystal formation begins in the bulk of the melt after the Na_3RuO_4 incorporation, in agreement with the mechanism we propose to explain the formation of needle-like RuO_2 crystals (Figure 12b).

The other hypothesis of needle-shape RuO_2 crystallization could be related to the precipitation of Ru, previously dissolved in a mix of nitrate and nitrite, during chemical reaction with glass frit (Figure 1a). Some Ru^{IV} dissolved in the region enriched in sodium in the melt could precipitate when sodium diffuses completely in the glass melt and thus decreases the local O^{2-} activity. To support this hypothesis, we will carry out complementary ESEM experiments to observe the reaction between a glass frit and a NaRu compound without Na_3RuO_4 precipitated.

5. CONCLUSION

Considerations of the chemistry of ruthenium in oxidized melts have allowed us to identify the key parameters and propose the mechanisms of formation of RuO_2 particles with acicular or polyhedral shapes during the synthesis of a simplified sodium borosilicate glass (Figure 12). The formation of polyhedral crystals is the result of the direct incorporation and dissolution of RuO_2 crystals in the melt followed by an Ostwald ripening mechanism. The formation of acicular crystals is associated with the presence of Ru^V as $Na_3Ru^VO_4$ in the melt. The dissolution of this compound in the borosilicate melt leads to the formation of ruthenium content, pO_2, and O^{2-} activity gradients. These gradients account for the precipitation of needle-like RuO_2 crystals.

This study helps to understand the formation of acicular and polyhedral particles in the complex SON68-type containment glass. The use of a variety of structural and microstructural characterization techniques made it possible to identify the steps in the formation of ruthenium compounds ($Na_3Ru^VO_4$) in a simplified calcined waste containing sodium nitrate and ruthenium dioxide. The presence of this ruthenate compound in the simplified waste containing precursor is the key parameter that controls further acicular RuO_2 crystallization in sodium borosilicate melts.

■ ASSOCIATED CONTENT

Supporting Information

The XRD spectrum of NaRu-top sample (S1), the video of the reaction between $NaNO_3$ and RuO_2 performed in situ in the

dx.doi.org/10.1021/ic202156y | Inorg. Chem. 2012, 51, 3478−3489

HT-ESEM chamber (S2), the differential thermal analyses (DTA) and weight loss of NaRu sample (S3), the video of the reaction between NaRu and glass frit performed *in situ* in the HT-ESEM chamber (S4), the video of the reaction between Na_3RuO_4 and glass frit performed *in situ* in the HT-ESEM chamber (S5), the video of the reaction between RuO_2 and glass frit performed *in situ* in the HT-ESEM chamber (S6), the EXAFS spectrum and relative Fourier transform of the SBN1-$NaRu_{800}$ and SBN1-$NaRu_{1300}$ cooled to room temperature (S7), and the video of the reaction between $NaNO_3$, RuO_2 and glass frit performed *in situ* in the HT-ESEM chamber (S8). This material is available free of charge via the Internet at http://pubs.acs.org.

AUTHOR INFORMATION

Corresponding Author

*E-mail: hassiba.boucetta@cea.fr.

Notes

The authors declare no competing financial interest.

ACKNOWLEDGMENTS

This work was financed by the Commissariat à l'Énergie Atomique et aux Énergies Alternatives. Financial support by AREVA is also gratefully acknowledged. The authors would like to thank the anonymous reviewers for their constructive comments, which have improved the quality of the manuscript. Access to synchrotron radiation facilities of ELETTRA (XAFS beamline) is acknowledged. The authors would like to thank L. Olivi and G. Aquilanti for expert advice on beamline operation.

REFERENCES

(1) Gras, J. M.; Do Quang, R.; Masson, H.; Lieven, T.; Ferry, C.; Poinssot, C.; Debes, M.; Delbecq, J. M. *J. Nucl. Mater.* **2007**, *362*, 383−394.

(2) Pinet, O.; Mure, S. *J. Non-Cryst. Solids* **2009**, *355*, 221−227.

(3) Galoisy, L.; Calas, G.; Morin, G.; Pugnet, S.; Fillet, C. *J. Mater. Res.* **1998**, *May*, 13.

(4) Gossé, S.; Schuller, S.; Guéneau, C. *Mater. Res. Soc. Symp. Proc.* **2010**, *1265*, 103−108.

(5) Gossé, S.; Guéneau, C. *Intermetallics* **2011**, *19*, 621−629.

(6) Demin, A. V.; Fedorova, M. I.; Matyunin, Y. I. *Atom. Energy* **1996**, *80*.

(7) Akai, T.; Nishii, J.; Yamashita, M.; Yamanaka, H. *J. Non-Cryst. Solids* **1997**, *222*, 304−309.

(8) Mitamura, H.; Murakami, T.; Banba, T.; Kiriyama, Y.; Kamizono, H.; Kumata, M.; Tashiro, S. *Nucl. Chem. Waste Manage.* **1983**, *4*, 245−251.

(9) Gong, W.; Lutze, W.; Matlack, K. S.; Pegg, I. L. *Glass Technol.: Eur. J. Glass Sci. Technol. A* **2009**, *50*, 95−107.

(10) Sundaram, S. K.; MacIsaac, B. C.; Cooper, A. R.; Trader, C. H.; Holbrook, J. J. *PNNL-13681* **2002**.

(11) Demin, A. V.; Matyunin, Y. I. *Atom. Energy* **1995**, *79*, 443−446.

(12) Krause, C.; Luckscheiter, B. *J. Mater. Res.* **1991**, *6*, 2535−2546.

(13) Igarashi, H.; Takahashi, T. *Glass Technol.* **1991**, *32*, 46−50.

(14) Igarashi, H.; Kawamura, K.; Takahashi, A. *Mater. Res. Soc.* **1992**, *257*, 169−176.

(15) Bart, F.; Dussossoy, J. L.; Fillet, C. *Mater. Res. Soc. Proc.* **2001**, *663*.

(16) Plodinec, M. J. *Adv. Ceram., Am. Ceram. Soc.* **1986**, *20*, 161−167.

(17) Mukerji, J.; Biswas, S. R. *Glass Ceram. Bull.* **1968**, *15*, 99−103.

(18) Mukerji, J.; Biswas, S. R. *Glass Ceram. Bull.* **1967**, *14*, 30−34.

(19) Prabhu, A.; Fuller, G. L.; Vest, R. W. *J. Am. Ceram. Soc.—Discuss. Notes* **1974**, *57*, 408−409.

(20) Borisov, A.; Nachtweyh, K. *Lunar Planetary Sci. Conference* **1998**, *XXIX*, abstract no. 1320.

(21) Bickford, D. F.; Jantzen, C. M. *J. Non-Cryst. Solids* **1986**, *84*, 209−307.

(22) Schreiber, H. D.; Settle, F. A. J.; Jamison, P. L.; Eckenrode, J. P.; Headley, G. W. *J. Less-Common Metals* **1986**, *115*, 145−154.

(23) Pflieger, R.; Lefebvre, L.; Malki, M.; Allix, M.; Grandjean, A. *J. Nucl. Mater.* **2009**, *389*, 450−457.

(24) Enokida, Y.; Sawada, K.; Uruga, K. Waste Man. 2009 Conference, Phoenix, AZ, March 2009.

(25) Enokida, Y. Waste Man. 2010 Conference, Phoenix, AZ, 2010

(26) Ogawa, T. *J. Am. Ceram. Soc.* **2010**, 1−4.

(27) Pflieger, R.; Malki, M.; Guari, Y.; Larionova, J.; Grandjean, A. *J. Am. Ceram. Soc.* **2009**, *92*, 1560−1566.

(28) Simonnet, C.; Grandjean, A. *J. Non-Cryst. Solids* **2005**, *351*, 1611−1618.

(29) Simonnet, C.; Grandjean, A.; Phalippou, J. *J. Nucl. Mater.* **2005**, *336*, 243−250.

(30) Rose, P. B.; Woodward, D. I.; Ojovan, M. I.; Hyatt, N.; Lee, W. E. *J. Non-Cryst. Solids* **2011**, *357*, 2989−3001.

(31) Shimada, T.; Sawada, K.; Hirabayashi, D.; Enokida, Y. *Proc. GLOBAL* **2011**.

(32) Advocat, T.; Jollivet, P.; Crovisier, J. L.; Del Nero, M. *J. Nucl. Mater.* **2001**, *298*, 55−62.

(33) Ravel, B.; Newville, M. *J. Synchr. Rad.* **2005**, *12*, 537−541.

(34) Newville, M. *J. Synchr. Rad.* **2001**, *8*, 322−324.

(35) Rehr, J. J.; Zabinsky, S. I.; Albers, R. C. *Phys. Rev. Lett.* **1992**, *69*, 3397−3400.

(36) Podor, R.; Clavier, N.; Ravaux, J.; Claparede, L.; Dacheux, N.; Bernache-Assollant, D. *J. Eur. Ceram. Soc.* **2012**, *32*, 353−362.

(37) Boman, C. E. *Acta Chem. Scan* **1970**, *24*, 116−122.

(38) Regan, K. A.; Huang, Q.; Cava, R. J. *J. Solid State Chem.* **2005**, *178*, 2104−2108.

(39) Abe, O.; Utsunomiya, T.; Hishino, Y. *J. Therm. Anal.* **1983**, *27*, 104−111.

(40) Shikano, M.; Kremer, R. K.; Ahrens, M.; Koo, H. J.; Whangbo, M. H.; Darriet, J. *Inorg. Chem.* **2004**, *43*, 5−7.

(41) Mogare, K. M.; Friese, K.; Klein, W.; Jansen, M. *Z. Anorg. Allg. Chem.* **2004**, *630*, 547−552.

(42) Berg, R. W.; Kerridge, D. H.; Larsen, P. H. *J. Chem. Eng. Data* **2006**, *51*, 34−39.

(43) Nakano, T.; Suzuki, K.; Yamaguchi, T. *J. Adhes.* **1994**, *46*, 131−144.

(44) Tilquin, J. Y.; Duveiller, P.; Gilbert, J.; Claes, P. *J. Non-Cryst. Solids* **1997**, *211*, 95−104.

(45) Khedim, H.; Podor, R.; Rapin, C.; Vilasi, M. *J. Am. Ceram. Soc.* **2008**, *91*, 3571−3579.

(46) Khedim, H.; Katrina, T.; Podor, R.; Panteix, P. J.; Rapin, C.; Vilasi, M. *J. Am. Ceram. Soc.* **2010**, *93*, 1347−1354.

(47) Khedim, H.; Podor, R.; Panteix, P. J.; Rapin, C.; Vilasi, M. *J. Non Cryst. Solids* **2010**, *356*, 2734−2741.

(48) Zarzyscki, J. *Les verres et l'état vitreux*; Masson Eds: Paris, 1982.

(49) Rard, J. A. *Chem. Rev.* **1985**, *85*, 1−39.

(50) Borisov, A.; Palme, H. *Am. Mineral.* **2000**, *85*, 1665−1673.

(51) Colson, R. O.; Malum, K. M. *Lunar Planetary Sci. Conference* **2005**, *XXXVI*, abstract no. 1190.

(52) Capobianco, C. G.; Hervig, R. L. *Lunar Planetary Sci.* **1996**, *XXVII*, 197−198.

(53) Mukerji, J.; Biswas, S. R. *Glass Technol.* **1971**, *12*, 107−112.

(54) Mukerji, J. *Glass Technol.* **1972**, *13*, 135−137.

(55) Ostwald, W. *Lehrbuch der Allgemeinen Chemie*; Leipzig, W. Engelmann, 1896; Vol. *2*.

(56) Li, W. J.; Shi, E. W.; Zhong, W. Z.; Yin, Z. W. *J. Cryst. Growth* **1999**, *203*, 186−196.

(57) Zhang, S.; Yao, S.; Li, J.; Zhao, L.; Wang, J.; Boughton, R. I. *J. Cryst. Growth* **2011**, *336*, 56−59.

(58) Khedim, H.; Abdelouhab, S.; Podor, R.; Rapin, C.; Vilasi, M.; Panteix, P. J.; Toplis, M.; Faure, F. *J. Non-Cryst. Solids* **2011**, *357*, 31−42.